ADVANCED FUNCTIONAL MATERIALS
www.afm-journal.de

Materials Views
www.MaterialsViews.com

High-Performance Metal-Free Solar Cells Using Stamp Transfer Printed Vapor Phase Polymerized Poly(3,4-Ethylenedioxythiophene) Top Anodes

Xiangjun Wang, Thilini Ishwara, Wei Gong, Mariano Campoy-Quiles, Jenny Nelson, and Donal D. C. Bradley**

The use of vapor phase polymerized poly(3,4-ethylenedioxythiophene) (VPP-PEDOT) as a metal-replacement top anode for inverted solar cells is reported. Devices with both i) standard bulk heterojunction blends of poly(3-hexylthiophene) (P3HT) donor and 1-(3-methoxycarbonyl)-propyl-1-phenyl-(6,6)C_{60} (PCBM) soluble fullerene acceptor and ii) hybrid inorganic/organic TiO_2/P3HT acceptor/donor active layers are studied. Stamp transfer printing methods are used to deposit both the VPP-PEDOT top anode and a work function enhancing PEDOT:polystyrenesulphonate (PEDOT:PSS) interlayer. The metal-free devices perform comparably to conventional devices with an evaporated metal top anode, yielding power conversion efficiencies of 3% for bulk heterojunction blend and 0.6% for organic/inorganic hybrid structures. These encouraging results suggest that stamp transfer printed VPP-PEDOT provides a useful addition to the electrode materials tool-box available for low temperature and non-vacuum solar cell fabrication.

1. Introduction

The use of transparent conducting polymers as electrode materials to complement and/or replace metal oxides (e.g., indium tin oxide (ITO)) and metals in optoelectronic devices has attracted considerable scientific and technological interest.[1–12] This is not only because of the notable improvements in conductivity, transparency, and chemical stability over recent years, but also the intrinsic advantages of these materials in terms of ease of processing, abundance, cost, and mechanical flexibility. In an early paper, polyaniline (PANI) was evaluated as an ITO replacement for polymer light-emitting diodes (PLEDs) on polyethylene terephthalate (PET) substrates.[1] However the absorption coefficient of PANI is high over the visible wavelength range and it is also chemically less stable than ITO. Subsequently the commercialized water dispersion of poly(3,4-ethylenedioxythiophene) decorated polystyrenesulphonate (PEDOT:PSS) was applied to ITO as an anode injection/extraction layer for organic light-emitting diodes (OLEDs)/organic photovoltaic (OPV) devices, respectively. Its positive effect on hole injection/extraction is attributed to its ability to planarise the ITO surface and increase its work function.[2] Standard injection/extraction layer PEDOT:PSS formulations (Clevios P VP CH8000 and P VP AI4083) have low conductivity (in the range 3×10^{-6} to 2×10^{-3} S cm^{-1}) and are thus not suited to outright ITO replacement. Conductivity enhancements of more than two orders of magnitude were later achieved by doping the PEDOT:PSS solution with compounds such as mesoerythritol or sorbitol.[3,4] The films deposited from these solutions have been used as ITO-replacement electrodes in OLEDs and OPV devices.[3–7] However, the performance of such devices lags that of conventional ITO based devices due to the much larger anode resistance. Newly commercialized Clevios PH 1000 offers conductivities of about 700 S cm^{-1} (albeit requiring the use of additives such as dimethylsulfoxide), allowing devices with performance closer to that of conventional ITO anode devices, especially for very small device areas.[7]

Vapor phase polymerized PEDOT (VPP-PEDOT) is another conducting polymer variant that has attracted strong interest[8–12] because of its promising conductivity and transparency. VPP-PEDOT layers on glass substrates have been used as anodes in photovoltaic devices, resulting in power conversion efficiency (PCE) values about one quarter of those obtained in conventional ITO based devices.[10] Improvements in the VPP synthesis process have led to a VPP-PEDOT conductivity of 1200 S cm^{-1} and thereby ITO-free PLEDs on glass with

Dr. X. Wang, Dr. T. Ishwara, W. Gong, Prof. J. Nelson, Prof. D. D. C. Bradley
Department of Physics and Centre for Plastic Electronics
The Blackett Laboratory
Imperial College London
SW7 2BZ London, UK
E-mail: jenny.nelson@imperial.ac.uk; d.bradley@imperial.ac.uk
W. Gong
Key Laboratory of Luminescence and Optical Information
Ministry of Education and Institute of Optoelectronic Technology
Beijing Jiaotong University
Beijing 100044, P. R. China
Dr. M. Campoy-Quiles
Institut de Ciència de Materials de Barcelona
UAB Campus, 08193 Bellaterra, Spain

DOI: 10.1002/adfm.201101787

performance comparable to otherwise equivalent ITO-based devices, likely also helped by better light out-coupling due to the lower refractive index of VPP-PEDOT.[11–12] Ideally, the conductivity of VPP-PEDOT should be further increased, while retaining adequate transmission, in order to have a good prospect of displacing ITO. For example, a conductivity of 5000 S cm^{-1} would allow a sheet resistance of 20 Ω $square^{-1}$ for a film thickness of 100 nm— values that would be attractive, especially if achieved on flexible substrates. Gadisa et al.[10] used a rubber stamp to deposit a VPP-PEDOT film as a top cathode electrode on a polymer:fullerene bulk heterojunction active layer in an OPV device. The resulting PCE was two orders of magnitude lower than that for reference devices with Al cathodes evaporated on top, in place of the VPP-PEDOT. The authors attributed this disappointing performance to the relatively low bulk conductivity of the VPP-PEDOT that they used (330–385 S cm^{-1}) and to a poor-quality contact at the VPP-PEDOT/active layer interface. One factor may be limited adhesion of the VPP-PEDOT layer to the polymer/fullerene active layer, leading to a weak physical attachment. Gadisa et al. present a photocurrent map of a typical 2 mm × 4 mm area device that indicates contact across the whole area (no dark spots are seen), although there is significant non-uniformity (±60% variation in photocurrent).[10]

Stamp transfer printing[13–14] and other more complicated solid film transfer techniques[15] have been further developed for optoelectronic device applications and used to fabricate multilayer structures with well-defined organic/organic interfaces. We have applied stamp transfer printed VPP-PEDOT layers to a wide variety of surfaces and used the method to fabricate a range of different devices in order to explore the opportunities for its application and to optimize device performance. Here we report the use of VPP-PEDOT as an anode (made more hole selective by the addition of a PEDOT:PSS work function enhancing interlayer) for inverted OPV devices. In the latter inverted architecture the cathode is placed at the bottom of the structure and is selected from materials other than the typically reactive metals used for regular top cathode devices. In particular, we study three types of inverted OPV device with charge generation regions comprising: i) hybrid inorganic:organic TiO_2:poly(3-hexylthiophene) (P3HT) bilayers, ii) hybrid inorganic:organic TiO_2:P3HT bilayers containing nanoporous TiO_2, in some cases coated with a monolayer of dye, and iii) bulk heterojunction blends of P3HT and 1-(3-methoxycarbonyl)-propyl-1-phenyl-(6,6)C_{60} (PCBM). In all cases the bottom cathode was ITO, made more electron-selective by the presence of a TiO_2 overlayer that also acts in device types (i) and (ii) as the primary acceptor for photocharge generation. In each case we compare the performance of the VPP-PEDOT anode devices with reference Au anode devices and discuss their relative merits. We demonstrate that metal-free VPP-PEDOT based devices can perform as well as their metal anode analogues thereby motivating the continued development of VPP-PEDOT as a novel electrode material.

2. Results and Discussion

The hybrid inorganic:organic inverted OPV devices (types (i) and (ii)) were fabricated as follows (further details are given in the Experimental Section). Substrates composed of ITO-on-glass were first coated with a layer of dense TiO_2 (denoted TiO_2(D)) that blocks holes from reaching the ITO cathode. The photocharge generation layer consisted of either this dense TiO_2 layer alone as acceptor with P3HT coated on top as donor (type (i)), or this dense TiO_2 layer first coated with a nanoporous TiO_2 adlayer as acceptor (denoted TiO_2(P), pore size 15–20 nm) with P3HT again coated on top as donor (type (ii)). In addition, for some type (ii) devices a monolayer of Z907 dye (*cis*-RuLL′$(SCN)_2$ with ligands L = 4,4′-dicarboxylic acid-2,2′-bipyridine and L′ = 4,4′-dinonyl-2,2′-bipyridine)[16] was adsorbed onto the TiO_2(P) layer before depositing the P3HT. Finally PEDOT:PSS and VPP-PEDOT were deposited on top by sequential stamp transfer printing. The resulting hybrid OPV devices are labelled as follows: Devices A: glass/ITO/TiO_2(D)/P3HT/PEDOT:PSS/VPP-PEDOT (i.e., type (i) bilayer hybrid VPP device); Devices B: glass/ITO/TiO_2(D)/TiO_2(P)/P3HT/PEDOT:PSS/VPP-PEDOT (i.e., type (ii) nanoporous hybrid VPP device); and Devices C: glass/ITO/TiO_2(D)/TiO_2(P)/Z907/P3HT/PEDOT:PSS/VPP-PEDOT (i.e., type (ii) nanoporous with dye hybrid VPP device).

Reference devices with Au as anode in place of VPP-PEDOT (but otherwise equivalent to Devices A, B, and C) were also fabricated and these are denoted A*, B*, and C*. External quantum efficiency (EQE) spectra were measured as described in the Experimental Section. The results for Devices A/A*, B/B*, and C/C* are depicted in **Figure 1**a.

The EQE of Devices A and A* show very similar performance, both spectrally and in terms of EQE magnitude. There are two EQE peaks at ≈340 nm and 480 nm, the latter with vibronic structure to longer wavelengths. These peaks can be assigned to photoinduced current generation dominated by excitation of TiO_2 and P3HT, respectively.[17,18] The EQE values are rather low (1% and 2% for the short and long wavelength peaks, respectively), behavior that is understood to be the result of a limited interfacial area for charge separation at the planar TiO_2:P3HT surface. The EQE long wavelength peak value (at 480 nm) increased by a factor of ≈5 upon insertion of the nanoporous TiO_2 layer in devices B (to ≈11% EQE) and B* (to ≈9% EQE). The increased photocurrent response relative to the planar bilayer structures can be explained by the enhanced TiO_2(P):P3HT interfacial area, giving rise to greater opportunities for charge separation. A further enhancement in EQE to 15.5% was obtained upon insertion of a thin layer of dye at the TiO_2(P)/P3HT interface in devices C and C*. A simple increase in absorption due the presence of the dye cannot be considered to be a major contribution to this enhancement since the absorption increment for the monolayer dye coating is small compared to the total absorption of the P3HT film. More importantly, as discussed further below, this enhancement is related to the energy levels of the dye favoring charge separation.

Comparison of the VPP-PEDOT based devices A, B, and C with their Au reference devices A*, B*, and C* showed that both of the VPP-PEDOT top anode, nanoporous TiO_2 devices (B and C) had higher EQEs than the corresponding Au reference devices (B* and C*) while for the VPP-PEDOT and Au capped planar bilayer (A and A*) devices the EQE values were very similar, though again, if anything, the VPP-PEDOT devices had slightly higher EQEs. The higher EQE for the VPP-PEDOT

ADVANCED FUNCTIONAL MATERIALS
www.afm-journal.de

Materials Views
www.MaterialsViews.com

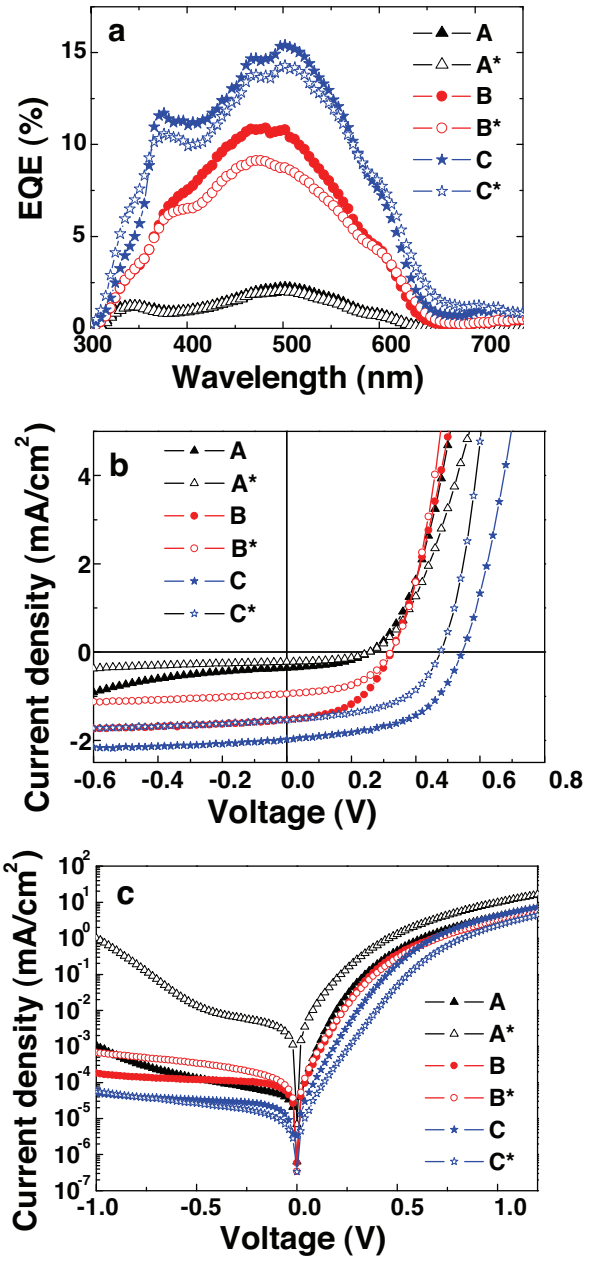

Figure 1. a) EQE spectra for (A/A*) planar bilayer hybrid devices (filled/open triangles correspond to VPP-PEDOT/Au anode devices and the line is a guide to the eye. The same convention is used for the other device data), (B/B*) nanoporous hybrid devices (filled/open circles and line), and (C/C*) nanoporous hybrid with Z907 dye devices (filled/open stars and line). b) *J–V* characteristics for devices A/A* (filled/open triangles and line), B/B* (filled/open circles and line), and C/C* (filled/open stars and line) under AM 1.5, 100 mW cm^{-2} illumination. c) The corresponding dark *J–V* data plotted on a semilogarithmic scale.

electrode devices suggests improved charge collection efficiency by VPP-PEDOT relative to Au, which could be due to a more uniform contact over the PEDOT:PSS surface. As reported below, the devices containing nanoporous TiO_2 have rough surfaces that might result in non-uniform coating by the evaporated Au layer during thermal deposition in vacuo.

The current density–voltage (*J–V*) characteristics for all of the hybrid device types under AM 1.5 simulated solar radiation (100 mW cm^{-2}) are presented in Figure 1b. **Table 1** lists the measured values of short circuit current density (J_{sc}), open circuit voltage (V_{oc}), fill factor (FF), and power conversion efficiency (PCE). PCE values increase with device complexity, independent of anode type (PCE(C) > PCE(B) > PCE(A) and PCE(C*) > PCE(B*) > PCE(A*)), but the VPP-PEDOT anode devices are consistently more efficient than their Au anode analogues (PCE(A) > PCE(A*), PCE(B) > PCE(B*) and PCE(C) > PCE(C*), even if only marginally so in the case of A/A*. The J_{sc} values similarly increase within each anode series (J_{sc}(C) > J_{sc}(B) > J_{sc}(A) for VPP-PEDOT anodes and J_{sc}(C*) > J_{sc}(B*) > J_{sc}(A*) for Au anodes) and are higher for VPP-PEDOT anodes than for Au anodes. The V_{oc} and FF values also increase within each anode series (A to B to C and A* to B* to C*) but the V_{oc} and FF values for VPP-PEDOT anode devices (A, B, and C) are not much different to those for the corresponding Au anode devices (A*, B*, and C*), though perhaps there is a slightly higher V_{oc} for the VPP-PEDOT anode devices. Therefore the increase in overall PCE for devices A, B, and C relative to devices A*, B* and C* is mainly due to the increase in J_{sc}. The greater enhancement in J_{sc} for the nanoporous TiO_2 containing devices B and C compared to B* and C* than that in device A compared to A* may indicate that VPP-PEDOT electrodes are more tolerant of surface roughness. The surfaces of the nanoporous TiO_2 based structures showed features with lateral dimensions of 10 s to 100 s of nanometers (atomic force microscopy image not shown here).

The observed V_{oc} difference of ≈100 mV between Devices A (A*) and B (B*) was surprising, given that the donor and acceptor materials and electrodes were the same and that it is widely believed that V_{oc} is limited by the lowest unoccupied molecular orbital (LUMO) (or conduction band edge) of the electron acceptor and the highest occupied molecular orbital (HOMO) of the electron donor[19,20] provided that contacts between donor and anode and between acceptor and cathode are ohmic.[19] The increase in photocurrent by a factor of 5 is insufficient to explain the observed increase in V_{oc}.[21] However, the improved V_{oc} is correlated to a lower dark leakage current in B (B*) compared to A (A*) (see Figure 1b,c) which may result from more efficient hole blocking through inclusion of the extra nanoporous TiO_2 layer (220 nm) in B (B*). More interesting are the further increases in J_{sc} and V_{oc} (by more than 150 mV) that were obtained upon insertion of a monolayer of dye (Z907) between the nanoporous TiO_2 and P3HT in devices C (C*). The enhanced device characteristics can be attributed to several effects caused by the Z907 dye: i) the amphiphilic Z907 improves wetting of the TiO_2 surface by the polymer; ii) the suitable LUMO level of Z907 positively mediates electron transfer from P3HT to TiO_2, enhancing J_{sc}; and iii) as shown in a previous study addition of the dye suppresses charge recombination (possibly due to the insulating effect of the dye's alkyl side chains) and thus improves V_{oc}.[16] Consistent with this, a decreased reverse bias dark current was found in Devices C (C*) as compared to B (B*) suggesting an improved hole blocking function. The same effect is not, however, plausible to explain the difference in V_{oc} between Devices C and C*, both of which have a Z907 dye layer and very similar reverse bias dark

Table 1. Summary photovoltaic data for hybrid and bulk heterojunction devices under AM1.5, 100 mW cm^{-2} illumination.

Device Type	Bottom electrode	Active layer	Top electrode	J_{sc} [mA cm^{-2}]	V_{oc} [V]	FF	PCE [%]
A	ITO	TiO_2(D)/P3HT	PEDOT:PSS/VPP-PEDOT	0.31 ± 0.03	0.26 ± 0.02	0.42 ± 0.02	0.03 ± 0.01
A*	ITO	TiO_2(D)/P3HT	PEDOT:PSS/Au	0.22 ± 0.02	0.25 ± 0.02	0.47 ± 0.01	0.02 ± 0.01
B	ITO	TiO_2(D)/TiO_2(P)/P3HT	PEDOT:PSS/VPP-PEDOT	1.57 ± 0.1	0.35 ± 0.04	0.50 ± 0.03	0.27 ± 0.02
B*	ITO	TiO_2(D))/TiO_2(P)/P3HT	PEDOT:PSS/Au	0.95 ± 0.04	0.32 ± 0.05	0.50 ± 0.01	0.15 ± 0.02
C	ITO	TiO_2(D)/TiO_2(P)/Dye/P3HT	PEDOT:PSS/VPP-PEDOT	1.97 ± 0.07	0.54 ± 0.02	0.54 ± 0.01	0.57 ± 0.02
C*	ITO	TiO_2(D)/iO_2(P)/Dye/P3HT	PEDOT:PSS/Au	1.50 ± 0.05	0.48 ± 0.02	0.53 ± 0.02	0.38 ± 0.02
D	ITO/TiO_2(D)	P3HT:PCBM(≈150 nm)	PEDOT:PSS/VPP-PEDOT	8.27 ± 0.49	0.55 ± 0.01	0.54 ± 0.02	2.45 ± 0.07
	ITO/TiO_2(D)	P3HT:PCBM(≈215 nm)	PEDOT:PSS/VPP-PEDOT	8.41 ± 0.27	0.58 ± 0.002	0.53 ± 0.01	2.59 ± 0.28
	ITO/TiO_2(D)	P3HT:PCBM(≈315 nm)	PEDOT:PSS/VPP-PEDOT	9.46 ± 0.58	0.57 ± 0.006	0.50 ± 0.03	2.70 ± 0.35
D*	ITO/TiO_2(D)	P3HT:PCBM(≈150 nm)	PEDOT:PSS/Au	8.63 ± 0.21	0.56 ± 0.02	0.49 ± 0.02	2.36 ± 0.19
E	ITO/TiO_2(D)	P3HT:PCBM (≈150 nm)	PEDOT:PSS/VPP-PEDOT	8.11 ± 0.15	0.51 ± 0.01	0.51 ± 0.02	2.27 ± 0.20
E*	ITO/TiO_2(D)	P3HT:PCBM (≈150 nm)	PEDOT:PSS/Au	9.59 ± 0.18	0.54 ± 0.00	0.56 ± 0.01	2.85 ± 0.12

The data are presented as average values for more than 10 individual devices of each type with error bars given by the data spread.

currents. Finally, compared with reference Devices C* the VPP-PEDOT based Devices C showed higher values of J_{sc}, V_{oc}, and FF, resulting in the highest PCE of ≈0.57% (comparable with that previously reported).[22] In summary, therefore, the performance of hybrid solar cells with VPP-PEDOT as a top anode was consistently better than that of the corresponding reference solar cells with Au top anodes (Table 1).

In order to further demonstrate the potential of transfer printed VPP-PEDOT as an anode material, we have also investigated cells with a P3HT:PCBM bulk heterojunction active layer. These devices had an inverted architecture as well, with the bottom of the device stack a cathode structure comprising dense TiO_2 (30 nm) coated ITO as hole blocking/electron accepting and high conductivity layers, respectively. A P3HT:PCBM blend film (≈150 nm thick) was next deposited as the photogeneration layer, followed by a PEDOT:PSS interlayer and a VPP-PEDOT anode. Devices that were thermally annealed before (pre-annealed) and after (post-annealed) deposition of the PEDOT:PSS and VPP-PEDOT layers were compared. In summary, the structures are labelled as follows: Devices D: glass/ITO/TiO_2(D)/P3HT:PCBM/PEDOT-PSS/VPP-PEDOT (PRE) and Devices E: glass/ITO/TiO_2(D)/P3HT:PCBM/PEDOT-PSS/VPP-PEDOT (POST).

Reference devices with Au as anode in place of VPP-PEDOT (but otherwise equivalent to Devices D and E) were also fabricated and these are denoted D* and E*.

The EQE spectra of these P3HT:PCBM bulk heterojunction devices D/D* and E/E* were measured and are depicted in **Figure 2**a. First, it is clear that the EQE values obtained for all bulk heterojunction devices (D, D*, E, and E*) are substantially larger than for hybrid devices (A, A*, B, B*, C, and C*, as shown in Figure 1a) reflecting the larger interfacial area available for exciton dissociation in the polymer:fullerene system than in the hybrid case. The bulk heterojunction device EQE spectra all peak at 505–515 nm with a maximum of 50% for D, E, and D* devices and 54% for the E* device. All EQE spectra have a shoulder at ≈595 nm, characteristic of the absorption of regioregular P3HT. The photogenerated current originates mainly from absorption in P3HT and exciton dissociation at the distributed P3HT:PCBM interfaces. The EQE is generally higher for the gold electrode devices (D* and E*) than for the VPP-PEDOT contacted (D and E) equivalents, especially in the 500–650 nm range. The difference in EQE magnitude and spectral distribution between VPP-PEDOT and Au devices is assigned to different optical absorbance within the active layers in the presence of electrodes with different (spectrally varying) reflectivities, as explained below.

The *J*–*V* characteristics for all of the inverted bulk heterojunction device types under AM 1.5 simulated solar radiation (100 mW cm^{-2}) are presented in Figure 2b and Table 1 lists the measured values of J_{sc}, V_{oc}, FF, and PCE. The trend in J_{sc} values (8.30, 8.11, 8.71, and 9.58 mA cm^{-2} for D, E, D*, and E* devices) is consistent with the trend in EQE values (Figure 2a). The V_{oc} and FF values are fairly similar for VPP-PEDOT and Au devices (see Table 1 D vs D* and E vs E*). For the VPP-PEDOT devices, post-annealing reduced both V_{oc} and FF, suggesting that thermal treatment after electrode deposition may degrade the performance of the PEDOT:PSS/VPP-PEDOT anode. Pre-annealing appears, however, to be entirely compatible with the formation of a robust interface between the P3HT:PCBM blend layer and the PEDOT:PSS/VPP-PEDOT electrode, thereby enabling efficient charge extraction. For the Au contacted devices, post-annealing leads to better overall device performance, largely through increased J_{sc} and FF. The J_{sc} may be influenced by the different degree of reflection of light from the Au contact in pre- and post-annealed devices, due to different roughness and Au coverage, while FF and J_{sc} could both be influenced by the quality of electrical contact between blend layer and PEDOT:PSS in the two cases.

The similar fill factors for the VPP-PEDOT and reference Au devices suggest that the higher resistance VPP-PEDOT electrode (≈100 ohm square^{-1}, ≈0.2 ohm square^{-1} for the Au electrode) does not limit performance for these small area solar cells. This

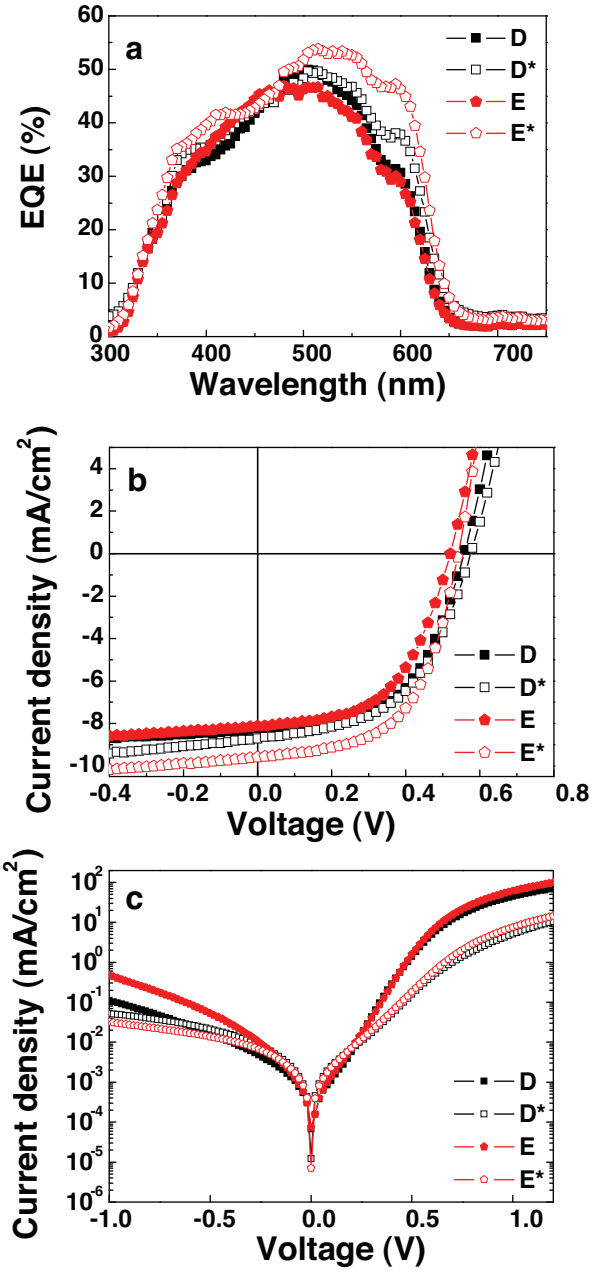

Figure 2. a) EQE spectra for pre-annealed (D/D*, filled/open squares) and post-annealed (E/E*, filled/open pentagons) inverted bulk heterojunction P3HT:PCBM devices. b) *J–V* characteristics for devices D/D* (filled/open squares) and E/E* (filled/open pentagons) under AM 1.5, 100 mW cm^{-2} illumination. c) The corresponding dark *J–V* data plotted on a semilogarithmic scale.

is supported by the device dark current data that show no evidence for higher series resistance in the VPP-PEDOT devices (Figure 2c). In fact, the diode quality is rather better for the VPP-PEDOT devices. Series resistance may, however, become a limiting factor for larger area devices, requiring the use of a grid of higher conductivity material.

To address the differences in spectral response for the VPP-PEDOT and Au electrode devices, we calculate the absorbance in the blend layers in each case, using a transfer matrix based optical model.[23] For this purpose, the real and imaginary parts of the complex dielectric function of the VPP-PEDOT layer were determined using spectroscopic ellipsometry (**Figure 3**a). Calculated spectra for optical absorbance within the blend layer in each structure are compared in Figure 3b. The results show that for 150 nm blend layers, the absorbance in VPP-PEDOT devices (solid line) is lower than that for Au devices (open triangles) both in the 350–450 nm range and especially in the 500–650 nm range. Analysis of the optical fields within the structure shows that the electromagnetic field strength is higher in the Au device, due to reflection from the electrode. Simulations (Figure 3b) show, however, that a thicker (315 nm) blend layer can be used to compensate for the absence of a reflective Au electrode. This was tested experimentally, by fabricating type D (pre-annealed, VPP-PEDOT electrode) devices with thicker P3HT:PCBM blend layers. Figure 3c shows the results for type D devices with 150 and 315 nm P3HT:PCBM layer thicknesses and for a control type D* (Au electrode) device with 150 nm P3HT:PCBM layer thickness. These confirm that the EQE and consequently J_{sc} values of the Au electrode device can be matched by a VPP-PEDOT electrode device with a thicker blend layer. Increasing the thickness of the P3HT:PCBM layer to 315 nm increases both J_{sc} and V_{oc}, and improves overall performance (Table 1). This optimized device structure enables PCE ≈ 3.05% with J_{sc} = 10.04 mA cm^{-2}, V_{oc} = 0.576 V, and FF = 0.526 (see Figure 3d), comparable with typical type D* (150 nm P3HT:PCBM) pre-annealed Au device data. The enhanced performance of type E* post-annealed Au devices relative to type D* (pre-annealed) devices cannot be explained by our planar optical model. However, there may be differences in the degree of reflection from the rough Au contacts and in the quality of the blend layer/anode electrical contact in the two cases. Finally it should be noted that the relatively high absorbance of VPP-PEDOT layers in the infrared (Figure 3a) could limit the photocurrent quantum efficiency at long wavelengths in device structures where the VPP-PEDOT is also required to provide optical access, such as in transparent and/or tandem cell structures.

3. Conclusion

In conclusion, we have demonstrated the successful use of the conducting polymer VPP-PEDOT as a top anode to fabricate inverted, metal-free, hybrid photogeneration layer (TiO_2:P3HT) solar cells. Photovoltaic characterization showed that these metal-free, VPP-PEDOT top anode solar cells performed better than corresponding metal-based (Au anode) devices. In addition, we have shown that insertion of a monolayer of an amphiphilic ruthenium dye (Z907) between the TiO_2 acceptor and P3HT donor layers can improve the hybrid solar cell performance.

VPP-PEDOT was further used as a top anode for metal-free inverted P3HT:PCBM bulk heterojunction devices. Characterization of these devices showed that the VPP-PEDOT anode bulk heterojunction devices with TiO_2-coated ITO cathodes performed at least as well as corresponding metal anode devices, once the blend layer thickness had been optimized to compensate for the absorption enhancement due to the Au electrode's optical reflectivity. The suitability of VPP-PEDOT as

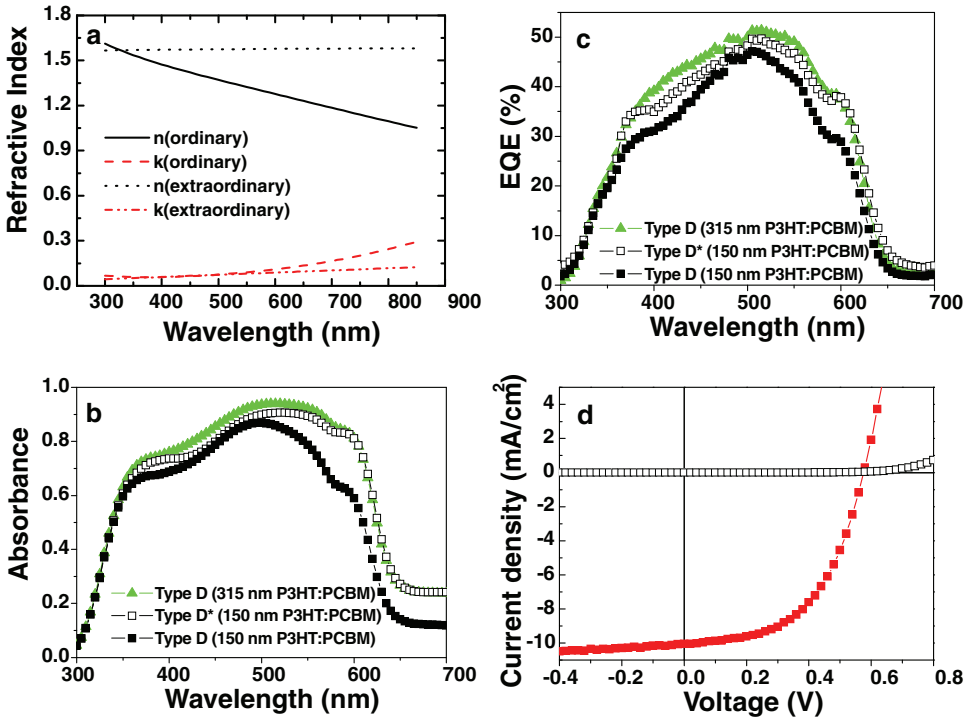

Figure 3. a) Refractive index (*n*) and extinction coefficient (*k*) spectra for a VPP-PEDOT layer on a silicon substrate. Both ordinary and extraordinary parts of the refractive index are shown. The ordinary parts were used in the optical modelling. The optical properties measured on Si substrates were similar to those measured on PEDOT:PSS. b) Calculated optical absorbance spectra for type D pre-annealed VPP-PEDOT electrode device structures with 150 nm (filled squares data and line) and 315 nm (filled triangles data and line) P3HT:PCBM blend layers and for a type D* pre-annealed Au electrode device with a 150 nm P3HT:PCBM blend layer (open squares data and line). c) Measured EQE spectra for type D pre-annealed VPP-PEDOT devices with 150 nm (filled squares data and line), and 315 nm (filled triangles data and line) P3HT:PCBM blend layers, and a type D* pre-annealed Au device with 150 nm P3HT:PCBM blend layer (open squares data and line). d) *J–V* characteristics for a type D pre-annealed VPP-PEDOT device with 315 nm P3HT:PCBM blend layer in the dark (open squares data) and under AM 1.5, 100 mW cm^{-2} illumination (filled squares data and line).

an anode arises from its high conductivity relative to other conducting polymers and the ability to deposit it via stamp transfer printing so as to form a robust contact with the PEDOT:PSS coated photogeneration layer, particularly where the latter has a rough surface. These results help to confirm the potential of VPP-PEDOT as an electrode material for use in optoelectronic devices and they encourage its further development.

4. Experimental Section

Materials: TiO_2 (from Dyesol), P3HT (from Merck Chemicals), PCBM (from API Services Inc), dye Z907 (from EPFL), and PEDOT:PSS (Baytron P VP AI4083 from H.C. Starck GmbH) were purchased and used without further purification. Patterned ITO-coated glass substrates (12 × 12 mm^2) were supplied by PsiOTec Ltd.

Inverted Hybrid Metal Oxide/Organic Semiconductor Solar Cells: Inverted hybrid metal oxide/organic semiconductor solar cells were fabricated from electron acceptor TiO_2 and electron donor P3HT layers. Dense, nanoporous and dye-coated nanoporous TiO_2 layers were employed for Devices A/A*, B/B*, and C/C*, respectively. For Devices A/A*, ITO-coated glass substrates (patterned to create a central ITO stripe) were first cleaned by ultrasonic agitation in acetone and isopropanol and then a dense TiO_2 (TiO_2(D)) layer (30 nm thickness) was coated on top of the ITO by spray pyrolysis.[24] For Devices B/B*, an additional nanoporous TiO_2 (TiO_2(P)) layer (220 nm thickness) was deposited on top of the TiO_2(D) layer of Devices A/A*, by spin coating colloidal TiO_2 particles (≈20 nm diameter) dissolved in tetrahydrofuran (THF) (110 mg mL^{-1}). Both TiO_2(D) and TiO_2(P) layers were annealed at 450 °C for 30 min in air. For Devices C/C*, the annealed glass/ITO/TiO_2(D)/TiO_2(P) structure was immersed in a dilute (0.3 mM) Z907 in butan-2-ol:acetonitrile (50:50 volume) solution for 2 h at 90 °C, then washed with the same solvent mixture to remove excess dye and dried under nitrogen flow. For Devices A/A*, the P3HT layer (≈140 nm thickness) was spin-coated directly onto the TiO_2(D) layer. For Devices B/B* and C/C*, the TiO_2(P) and TiO_2(P)-with-dye layers were pre-coated by immersion in a dilute P3HT in chlorobenzene (≈2 mg mL^{-1}) solution for 18 h at ≈110 °C and then dried by spinning in air. A layer of P3HT (≈140 nm thickness) was then spin-coated on top. Next, for each of Devices A/A*, B/B* and C/C*, a PEDOT:PSS layer (≈50 nm) was deposited on top of the spin-coated P3HT layer by stamp transfer printing. Our process for stamp transfer printing has been previously described in detail.[13] In brief, a polydimethylsiloxane (PDMS) stamp coated with the desired thickness of PEDOT:PSS was brought into physical contact with the underlying structure and pressed against it to ensure conformal contact. The stamp was then peeled back leaving the transferred film in place. Finally for Devices A, B and C stripe-patterned, ≈100 nm thickness VPP-PEDOT[11] contacts were stamp transfer printed on top of the PEDOT:PSS. The VPP-PEDOT films were synthesized on top of PDMS stamps using our standard procedure,[11,12] namely coating the PDMS with an oxidant solution and exposing it to ethylenedioxythiophene vapor within an enclosed, nitrogen atmosphere vessel. Patterning to form the required stripes was done using a spatially patterned PDMS stamp, with a surface relief in the form of the negative of the desired stripe pattern. This patterned stamp was pressed against the uniformly VPP-PEDOT coated flat PDMS stamp and on being peeled back removed the unwanted portions of the VPP-PEDOT film, leaving the desired contact stripes. The flat stamp was then used to transfer the stripes onto the PEDOT:PSS by pressing (with appropriate alignment) it against the PEDOT:PSS and then peeling away, as described above and previously.[13] For Devices A*, B*, and C* shadow mask defined Au contact stripes (100 nm thickness) were evaporated in vacuo (≈10^{-6} mbar) in place of the VPP-PEDOT. The solar cell area in all cases was ≈4.5 mm^2, defined by the overlap of the orthogonally aligned VPP-PEDOT or Au anode and ITO cathode stripes. Six individual devices were prepared on each substrate.

The resulting inverted hybrid metal-oxide/organic semiconductor solar cells are then as follows: Devices A (A*): glass/ITO/TiO_2(D)/P3HT/PEDOT:PSS/VPP-PEDOT (Au); Devices B (B*): glass/ITO/TiO_2(D)/TiO_2(P)/P3HT/PEDOT:PSS/VPP-PEDOT (Au); and Devices C (C*): glass/ITO/TiO_2(D)/TiO_2(P)/Z907/P3HT/PEDOT:PSS/VPP-PEDOT (Au).

Inverted Bulk Heterojunction P3HT:PCBM Blend Solar Cells: Inverted bulk heterojunction P3HT:PCBM (50:50 by weight) blend solar cell Devices D/D* and E/E* were fabricated using TiO_2(D) (30 nm thickness) coated ITO cathodes, prepared as described above. The P3HT:PCBM layer (150, 215, and 315 nm thickness) was spin-coated on top from chlorobenzene solution, with thickness controlled by spin-speed and solution concentration. Devices D/D* were pre-annealed, i.e., annealed at 140 °C for 1 h, before a PEDOT:PSS layer was stamp-transfer-printed on top (as described above). Devices D were completed by stamp transfer printing of stripe-patterned, VPP-PEDOT electrodes whilst Devices D* had shadow mask defined Au electrode stripes (as described above). Devices E/E* were post-annealed, i.e., annealed at 140 °C for 1 h after the PEDOT:PSS and VPP-PEDOT or Au layers had been deposited. The solar cell active area was in all cases ≈ 4.5 mm^2, defined by the overlap of orthogonally aligned VPP-PEDOT/Au and ITO stripes.

The resulting inverted bulk heterojunction P3HT:PCBM blend solar cells are then as follows: Devices D (D*): glass/ITO/TiO_2(D)/P3HT:PCBM/PEDOT:PSS/VPP-PEDOT (Au) pre-annealed before deposition of PEDOT:PSS and VPP-PEDOT (Au) and Devices E (E*): glass/ITO/TiO_2(D)/P3HT:PCBM/PEDOT:PSS/VPP-PEDOT (Au) post-annealed after deposition of PEDOT:PSS and VPP-PEDOT (Au).

Characterization: Film thicknesses were measured using a Tencor Instruments Alpha Step 200 surface profilometer.

J–V and photocurrent spectral characteristics were measured using a Keithley 238 Source Measure Unit GPIB-interfaced to a computer. A 300 W xenon arc lamp solar simulator (Oriel Instruments) with an AM1.5 output of 100 mW cm^{-2} was used for the light *J–V* measurements. Photocurrent spectra were recorded using the monochromated (Bentham) output from a Tungsten halogen source, calibrated with a Newport UV-181 photodiode. All measurements were carried out with illumination incident through the glass substrate. More than 10 individual cells were characterized for each of Devices A/A*, B/B*, C/C*, D/D*, and E/E* and the data reported in Table 1 are averages over these individual cells.

The sheet resistance of the conducting layers was measured using a four-point probe apparatus with current-voltage data recorded by a Keithley 2000 multimeter as described previously.[11]

A SOPRALAB rotating polarizer ellipsometer (GES-5E) with charge coupled device (CCD) detection, was used for variable angle spectroscopic ellipsometry (VASE) and further polarized transmission measurements on VPP-PEDOT samples deposited on silicon and quartz substrates. The complex refractive index was determined using multi-sample analysis for the combined VASE and transmission data. It was found that anisotropic refractive indices had to be employed in order to describe simultaneously all of the data, despite the fact that small variations in *n* and *k* were observed depending on film thickness, level of doping and substrate used. The complex refractive index was deduced using a standard dielectric function model comprising a Cauchy law term, one Lorentzian peak in the UV region, and a Drude tail in the IR.

Optical Modelling: A transfer matrix method was used to calculate the electromagnetic field strength within a planar multi-layer model device structure.[23] Complex refractive index data for the blend layer were taken from previous measurements of a P3HT:PCBM blend film.[25]

Acknowledgements

The UK authors thank the Royal Society Brian Mercer Bequest, the Engineering and Physical Sciences Research Council (EP/E045472, EP/F061757/1 and Knowledge Transfer Secondment scheme), and the Lee-Lucas Endowment for financial support. MCQ thanks the Spanish Ministry of Science and Innovation for funding through the Ramon y Cajal fellowship and project MAT2009-10642.

Received: August 2, 2011
Revised: November 28, 2011
Published online: February 2, 2012

[1] G. Gustafsson, Y. Cao, G. M. Treacy, F. Klavetter, N. Colaneri, A. J. Heeger, *Nature* **1992**, *357*, 477.
[2] a) S. A. Carter, M. Angelopoulos, S. Karg, P. J. Brock, J. C. Scott, *Appl. Phys. Lett.* **1997**, *70*, 2067; b) T. M. Brown, J. S. Kim, R. H. Friend, F. Cacialli, R. Daik, W. J. Feast, *Appl. Phys. Lett.* **1999**, *75*, 1679; c) P. Peumans, S. R. Forrest, *Appl. Phys. Lett.* **2001**, *79*, 126.
[3] a) F. Zhang, M. Johansson, M. R. Andersson, J. C. Hummelen, O. Inganäs, *Adv. Mater.* **2002**, *9*, 662; b) J. Ouyang, C. W. Chu, F. C. Chen, Q. Xu, Y. Yang, *Adv. Funct. Mater.* **2005**, *15*, 203.
[4] a) J. Huang, P. F. Miller, J. S. Wilson, J. C. De Mello, A. J. De Mello, D. D. C. Bradley, *Adv. Funct. Mater.* **2005**, *15*, 290; b) J. Huang, X. Wang, Y. Kim, A. J. deMello, D. D. C. Bradley, J. C. deMello, *Phys. Chem. Chem. Phys.* **2006**, *8*, 3904; c) P. Ravirajan, D. D. C. Bradley, J. Nelson, S. A. Haque, J. R. Durrant, H. J. P. Smit, J. M. Kroon. *Appl. Phys. Lett.* **2005**, *86*, 143101.
[5] K. Fehse, K. Walzer, K. Leo, W. Lovernich, A. Elschner, *Adv. Mater.* **2007**, *19*, 441.
[6] Y. Zhou, H. Cheun, S. Choi, W. J. Potscavage Jr., C. Fuentes-Hernandez, B. Kippelen, *Appl. Phys. Lett.* **2010**, *97*, 153304.
[7] Y.-F Lim, S. Lee, D. J. Herman, M. T. Lloyd, J. E. Anthony, G. G. Malliaras, *Appl. Phys. Lett.* **2008**, *93*, 193301.
[8] S. Admassie, F. Zhang, A.G. Manoj, M. Svensson, M. R. Andersson, O. Inganäs, *Sol. Energy Mater. Sol. Cells* **2006**, *90*, 133.
[9] B. Winther-Jensen, F. C. Krebs, *Sol. Energy Mater. Sol. Cells* **2006**, *90*, 123.
[10] A. Gadisa, K. Tvingstedt, S. Admassie, L. Lindell, X. Crispin, M. R. Andersson, W. R. Salaneck, O. Inganäs, *Synth. Met.* **2006**, *156*, 1102.
[11] P. A. Levermore, L. Chen, X. Wang, R. Das, D. D. C. Bradley, *Adv. Mater.* **2007**, *19*, 2379.
[12] P. A. Levermore, R. Jin, X. Wang, L. Chen, D. D. C. Bradley, J. C. de Mello, *J. Mater. Chem.* **2008**, *18*, 4414.
[13] L. Chen, P. Degenaar, D. D. C. Bradley, *Adv. Mater.* **2008**, *20*, 1679.
[14] T. A. M. Ferenczi, J. Nelson, C. Belton, A.M. Ballantyne, M. Campoy-Quiles, F. M. Braun, D. D. C. Bradley, *J. Phys. Condens. Matter* **2008**, *20*, 475203.
[15] K.-H. Yim, Z. Zheng, Z. Liang, R. H. Friend, W. T. S. Huck, J.-S. Kim, *Adv. Funct. Mater.* **2008**, *18*, 1.
[16] a) P. Ravirajan, A. M. Peiro, M. K. Nazeeruddin, M. Grätzel, D. D. C. Bradley, J. R. Durrant, J. Nelson, *J. Phys. Chem. B* **2006**, *110*, 7635; b) P. Ravirajan, S. A. Haque, J. R. Durrant, D. D. C. Bradley, J. Nelson, *Adv. Funct. Mater.* **2005**, *15*, 609–618; c) A. M. Peiro, P. Ravirajan, K. Govender, D. S. Boyle, P. O'Brien, D. D. C. Bradley, J. Nelson, J. R. Durrant, *J. Mater. Chem.* **2006**, *16*, 2088.
[17] a) P. Ravirajan, S. A. Haque, D. Poplavskyy, J. R. Durrant, D. D. C. Bradley, J. Nelson, *J. Appl. Phys.* **2004**, *95*, 1473; b) P. Ravirajan, S. A. Haque, D. Poplavskyy, J. R. Durrant, D. D. C. Bradley, J. Nelson, *Thin Solid Films* **2004**, *451-452*, 624.
[18] V. Shrotriya, J. Ouyang, R. J. Tseng, G. Li, Y. Yang, *Chem. Phys. Lett.* **2005**, *411*, 138.
[19] C. J. Brabec, A. Cravino, D. Meissner, N. S. Sariciftci, T. Fromherz, M. T. Rispens, L. Sanchez, J. C. Hummelen, *Adv. Funct. Mater.* **2001**, *11*, 374.
[20] V. D. Mihailetchi, P. W. M. Blom, J. C. Hummelen, M. T. Rispens, *J. Appl. Phys.* **2003**, *94*, 6849.
[21] T. Ishwara, D. D. C. Bradley, J. Nelson, P. Raviranjan, I. Vanseveren, T. Cleij, D. Vanderzande, L. Lutsen, S. Tierney, M. Heeney, I. McCulloch, *Appl. Phys. Lett.* **2008**, *92*, 053308–3
[22] C. Goh, S. R. Scully, M. D. McGehee, *J. Appl. Phys.* **2007**, *101*, 114503.
[23] a) F. Braun, PhD thesis, University of London 2007; b) L. A. A. Pettersson, L. S. Roman, O. Inganäs, *J. Appl. Phys.* **2001**, *89*, 5564.
[24] L. Kavan, M. Grätzel, *Electrochim. Acta* **1995**, *40*, 643.
[25] T. Agostinelli, S. Liliu, J. G. Labram, M. Campoy-Quiles, M. Hampton, E. Pires, J. Rawle, D. D. C. Bradley, T. D. Anthopoulos, J. Nelson, J. E. MacDonald, *Adv. Funct. Mater.* **2011**, *21*, 1701.